Structure function tensor scaling in the logarithmic region derived from the attached eddy model of wall-bounded turbulent flows

X. I. A. Yang,[1] R. Baidya,[2] P. Johnson,[1] I. Marusic,[2] and C. Meneveau[1]
[1]*Department of Mechanical Engineering, Johns Hopkins University, Baltimore, Maryland 21218, USA*
[2]*Department of Mechanical Engineering, University of Melbourne, Parkville, VIC, 3010, Australia*
(Received 9 March 2017; published 5 June 2017)

We investigate the scaling of the velocity structure function tensor $D_{ij}(\mathbf{r},z)$ in high Reynolds number wall-bounded turbulent flows, within the framework provided by the Townsend attached eddy hypothesis. Here $i,j = 1,2,3$ denote velocity components in the three Cartesian directions, and $\mathbf{r}$ is a general spatial displacement vector. We consider spatial homogeneous conditions in wall-parallel planes and dependence on wall-normal distance is denoted by z. At small scales ($r = |\mathbf{r}| \ll z$) where turbulence approaches local isotropy, $D_{ij}(\mathbf{r},z)$ can be fully characterized as a function of r and the height-dependent dissipation rate $\epsilon(z)$, using the classical Kolmogorov scalings. At larger distances in the logarithmic range, existing previous studies have focused mostly on the scaling of D_{ij} for $\mathbf{r}$ in the streamwise direction and for the streamwise velocity component ($i = j = 1$) only. No complete description is available for $D_{ij}(\mathbf{r},z)$ for all i,j, and $\mathbf{r}$ directions. In this paper we show that the hierarchical random additive process model for turbulent fluctuations in the logarithmic range (a model based on the Townsend's attached eddy hypothesis) may be used to make new predictions on the scaling of $D_{ij}(\mathbf{r},z)$ for all velocity components and in all two-point displacement directions. Some of the generalized scaling relations of $D_{ij}(\mathbf{r},z)$ in the logarithmic region are then compared to available data. Nevertheless, a number of predictions cannot yet be tested in detail, due to a lack of simultaneous two-point measurements with arbitrary cross-plane displacements, calling for further experiments to be conducted at high Reynolds numbers.

DOI: 10.1103/PhysRevFluids.2.064602

I. INTRODUCTION

The most basic statistical characterization of turbulence structure is encoded in the two-point correlation or two-point structure functions of the turbulent velocity field. At small scales, with displacements in the inertial range of turbulence, a universal form is available from the Kolmogorov scaling [1,2]. In wall-bounded flows, at scales comparable to the distance from the wall in the logarithmic region, very significant deviations from local isotropy develop. We lack a suitably general description of anisotropic energy containing motions, and the present work is devoted to this topic.

Wall-bounded flows, particularly flows at high Reynolds numbers, have been the subject of sustained research efforts (see, e.g., Refs. [3–5] for reviews), and predictive reduced-order models are extensively available in the literature [6–14]. A fairly established conceptual model for high Reynolds number wall-bounded turbulent flows is the Townsend attached eddy model [6], in which the logarithmic region is modeled as a collection of self-similar, wall-attached eddies, whose sizes scale with their distance from the wall (see Fig. 1). Despite its simple form, this model has been quite useful. Invoking the attached eddy hypothesis, not only can the logarithmic scaling of the mean velocity profile be derived, but Townsend [6] also derived the logarithmic scalings for $\langle u^2 \rangle \sim \log(\delta/z)$, $\langle v^2 \rangle \sim \log(\delta/z)$, where u and v are the velocity fluctuations in the streamwise and spanwise directions, δ is an outer length scale, and z is the wall-normal coordinate. To date, these two generalized logarithmic scalings have received considerable empirical support [15–19]. The attached eddy picture also permits scaling laws including $\langle \Delta u^2 \rangle \sim \log(r_x/z)$, $\langle u(x)u(x+r_x) \rangle \sim \log(\delta/r_x)$, which have been confirmed recently in de Silva *et al.* [20] and Yang *et al.* [21], respectively. Here

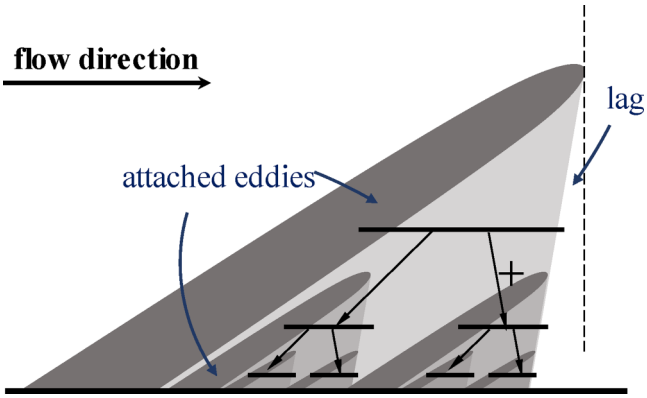

FIG. 1. Conceptual schematic diagram of the attached eddy model of high Reynolds number turbulent boundary layer flows. The number of visible eddies on a vertical cut doubles as the sizes of the eddies halve. An attached eddy affects the shaded region. A realization of the velocity fluctuation at a generic point in the flow field is given by a superposition of the velocity fields associated with the attached eddies within which the generic point locates. Inclination of the attached eddies leads to a lag in the velocity signal between two wall-normal locations, as indicated in the sketch.

$\Delta u = u(x + r_x) - u(x)$, r_x is a streamwise displacement and x is the streamwise coordinate. In addition to these logarithmic scalings, the k_x^{-1} spectrum in the logarithmic region is also a direct consequence of the presence of wall-attached eddies [22]. More recently, the attached-eddy model has been extended to account for more detailed observations, including wake effects and eddy clustering phenomena (see, e.g., Refs. [7,8]), as well as logarithmic scalings of higher order moments [20,23].

More generally, the statistics of turbulent flows are fully specified by all N-point M-order correlation functions [24], or equivalently, the related structure functions. Structure functions were found to be particularly useful for studying homogeneous isotropic turbulence, where an exact relation holds connecting the third-order structure function to the second order as a function of the dissipation rate [1]. Furthermore, we remark that knowledge of the scalings of the structure functions can be used to provide estimates on the coarse-grained velocity gradients, subfilter stresses, and higher order subscale cumulants [25–27], which has implications for subgrid-scale modeling and large-eddy simulations, where eddies of any particular scale in wall units become more and more subgrid (unresolved) as the Reynolds number increases. Moreover, a second-order spatial statistical description can be leveraged to model the full spatio-temporal structure [28,29] of the flow.

In this work we consider the two-point, second-order structure function defined as

$$D_{ij}(\mathbf{x},\mathbf{r}) = \langle (u_i(\mathbf{x}+\mathbf{r}) - u_i(\mathbf{x}))(u_j(\mathbf{x}+\mathbf{r}) - u_j(\mathbf{x}))\rangle. \tag{1}$$

For incompressible homogeneous isotropic turbulence, this tensor could be fully specified with a scalar function $D_{LL}(r)$ (the longitudinal structure function) [2,24], which in turn only depends on r and the mean rate of dissipation ϵ in the inertial range (with the formula being $D_{ij} = D_{LL}\delta_{ij} + r/2\partial D_{LL}/\partial r(\delta_{ij} - r_i r_j/r^2)$, where δ_{ij} is the second-order identity tensor). The local isotropic behavior is expected to hold in wall-bounded turbulence for displacements much smaller than the height z above the wall [20,30–32]. As the dissipation in the logarithmic region can be evaluated assuming equilibrium between production and dissipation, the z dependence of the longitudinal structure function is encoded in $\epsilon(z) \sim u_\tau^3/z$. On the other hand for displacements larger than the height ($r > z$), i.e., for the energy-containing and momentum-transporting motions, turbulence becomes anisotropic and inhomogeneous so that simplifications associated with isotropy are not possible, and the specification of the second-order structure functions becomes less simple.

Structure functions in wall-bounded flows have been considered from a theoretical viewpoint by Hill [33] and Cimarelli *et al.* [34] as part of derivations of a generalized Kolmogorov equation

allowing for nonhomogeneity and anisotropy. From an experimental viewpoint, structure functions have been studied in recent works by Davidson [32] and de Silva *et al.* [20]. These prior efforts have focused primarily on the streamwise direction, i.e., the special case $\mathbf{r} = (r_x,0,0)$ and $i = j = 1$.

The attached eddy model for energy containing motions in wall-bounded flows is analogous [35] to the eddy hierarchy cascade models for isotropic homogeneous turbulence [2]. It describes the statistical structure of turbulent motions in a given range by providing a method for calculating statistics based on randomly distributed wall-attached, momentum-transferring eddies with a chosen characteristic eddy shape, and a prescribed density depending on distance to the wall. As a result it allows for scaling predictions over a certain range of scales in wall-bounded turbulence. While previously, only scalings of the streamwise velocity component with streamwise displacements were considered in the attached eddy model, predictions can also be made for other velocity components included in other Reynolds stresses, as shown in Refs. [7,8]. However, for structure functions in arbitrary directions and for all three velocity components, scaling predictions have not yet been established based on the attached eddy model. Given the success of the model in the context of streamwise statistics, it is of interest to extend scaling predictions to other directions and velocity components. This is the main objective of the work presented here.

We develop predictions on the scalings of the full structure function tensor Eq. (1), for $\mathbf{x}$ in the logarithmic region and for relevant ranges of the two-point displacement $\mathbf{r}$ such that $\mathbf{x} + \mathbf{r}$ is also in the log region (see Ref. [36] for detailed discussion on the extent of the log region). u_i, u_j are the velocity fluctuations in x_i, x_j directions; $i, j = 1,2,3$. We first consider the full specification of a general second-order structure function under the specific conditions that the wall-normal coordinate is denoted by a unit vector $\hat{\mathbf{z}}$, and the direction of the free stream velocity is given by a unit vector $\hat{\mathbf{u}}$. Because of the translational symmetry on wall-parallel planes, the dependency of D_{ij} on $\mathbf{x}$ is reduced to $z = \mathbf{x} \cdot \hat{\mathbf{z}}$, where z is the wall-normal component of $\mathbf{x}$. The two-point displacement vector $\mathbf{r}$ may be in any direction. In general, the symmetric, $\hat{\mathbf{x}}$, $\hat{\mathbf{z}}$, and $\mathbf{r}$-dependent tensor D_{ij} may be expressed as

$$\begin{aligned} D_{ij}(\mathbf{r},z) = {} & D_{11}(r_x,r_y,r_z,z)\hat{u}_i\hat{u}_j + D_{12}(\cdot)(\hat{u}_i\hat{t}_j + \hat{u}_j\hat{t}_i) + D_{13}(\cdot)(\hat{u}_i\hat{z}_j + \hat{u}_j\hat{z}_i) + D_{22}(\cdot)\hat{t}_i\hat{t}_j \\ & + D_{23}(\cdot)(\hat{t}_i\hat{z}_j + \hat{t}_j\hat{z}_i) + D_{33}(\cdot)\hat{z}_i\hat{z}_j, \end{aligned} \tag{2}$$

where $\hat{\mathbf{t}} = \hat{\mathbf{z}} \times \hat{\mathbf{u}}$ (unit vectors $\hat{\mathbf{u}}$ and $\hat{\mathbf{z}}$ are orthogonal), $\hat{\mathbf{u}}$, $\hat{\mathbf{z}}$, and $\hat{\mathbf{t}}$ form a rectangular coordinate system, D_{11}, D_{12}, D_{13}, D_{22}, D_{13}, and D_{33} are scalar functions of z, $r_x = \mathbf{r} \cdot \hat{\mathbf{u}}$, $r_y = \mathbf{r} \cdot \hat{\mathbf{t}}$, $r_z = \mathbf{r} \cdot \hat{\mathbf{z}}$ and the friction velocity u_τ (or magnitude of the free-stream velocity). As D_{ij} is symmetric under coordinate system reflection, terms depending on $\hat{\mathbf{t}}$ have to vanish, i.e., $D_{12} = D_{23} = 0$. Note that according to the theory of homogeneous tensors, a symmetric tensor that depends on three vector ($\hat{\mathbf{z}}$, $\hat{\mathbf{u}}$, $\mathbf{r}$) takes the form

$$\begin{aligned} D_{ij}(\mathbf{r},z) = {} & f_\delta\delta_{ij} + f_{uu}\hat{u}_i\hat{u}_j + f_{zz}\hat{z}_i\hat{z}_j + f_{rr}\hat{r}_i\hat{r}_j + f_{ur}\tfrac{1}{2}(\hat{u}_i\hat{r}_j + \hat{u}_j\hat{r}_i) + f_{uz}\tfrac{1}{2}(\hat{u}_i\hat{z}_j + \hat{u}_j\hat{z}_i) \\ & + f_{zr}\tfrac{1}{2}(\hat{z}_i\hat{r}_j + \hat{z}_j\hat{r}_i), \end{aligned} \tag{3}$$

where the f are scalar functions of a number of scalar quantities that can be formed from the vectors $\mathbf{r}$, $\hat{\mathbf{u}}$, $\hat{\mathbf{z}}$ and the distance z. As a constraint in this problem, the vectors $\hat{\mathbf{u}}$ and $\hat{\mathbf{z}}$ are perpendicular to each other, introducing additional conditions. Since the above general tensor requires the specification of seven instead of four scalar functions [as in Eq. (2)], we opt to use Eq. (2).

Throughout the paper, we denote x_1, x_2, x_3 as the streamwise, spanwise, and wall-normal coordinates, respectively; we interchangeably use u, v, w for the velocity fluctuations in the streamwise, spanwise, and wall-normal directions; x, y, z are interchangeably used for x_1, x_2, x_3. As stated above, the displacement $\mathbf{r} = (r_x,r_y,r_z)$, and $r_z > 0$. In this paper, velocities are normalized by the friction velocity u_τ, and normalization with viscous length scale ν/u_τ (where ν is the kinematic viscosity) will be indicated by a $+$ superscript. We consider only velocity fluctuations. As mentioned before, prior work has focused mostly on the dependence of D_{11} upon r_x. As can be seen above, for the full specification of the generalized structure function, we also require expressions for the scalar functions D_{22}, D_{33}, and D_{13}, all as functions of (r_x,r_y,r_z,z). As shown by Hill [33], incompressibility

imposes the following constraint on the structure function:

$$\frac{\partial D_{ij}(\mathbf{r},z)}{\partial r_j} = \frac{1}{2}\frac{\partial}{\partial x_3}\langle[u_i(\mathbf{x}+\mathbf{r})+u_i(\mathbf{x})][u_3(\mathbf{x}+\mathbf{r})-u_3(\mathbf{x})]\rangle, \tag{4}$$

which involves moments other than the structure functions themselves, and thus we will not exploit incompressibility as a useful constraint.

In Sec. II, we summarize the hierarchical random additive process as a model for wall-bounded turbulent velocity fluctuations in the logarithmic range and in Sec. III show how it can be used to make predictions about the general scaling of these functions. We will invoke the simplest possible modeling assumptions and state the resulting specific predictions. We will then attempt to verify the predicted trends in Sec. IV. Several of the required measurements are available only from DNS at moderate to intermediate Reynolds numbers so the discussion in Sec. IV cannot be considered conclusive. We leave open the possibility that once measurements become available at high Reynolds numbers, the various simplifying assumptions made in the simplest version of the proposed model may need further refinement.

II. THE HIERARCHICAL RANDOM ADDITIVE PROCESS (HRAP) MODEL

The HRAP is a simplified version of the Townsend attached eddy model, in which the eddy-induced velocity fields are modeled as random addends. The wall-parallel velocity components at a wall-normal distance z include additive contributions from eddies whose heights are greater than z. Conversely, for the wall-normal component, the contributions from large eddies whose heights are greater than z are severely blocked by the presence of the wall, and only contributions from eddies of a size comparable to z count. Accordingly, the HRAP formalism models the instantaneous streamwise and spanwise velocity fluctuations at a given position and height z as a result of random additive processes according to

$$u = \sum_{i=1}^{N_z} a_i, \quad v = \sum_{i=1}^{N_z} b_i. \tag{5}$$

A random addend a_i (or b_i) represents the velocity increment in u (or v) due to an attached eddy of height $\sim\delta/2^i$, where δ is the height of the largest wall attached eddy that the boundary layer can admit (typically on the order of the outer boundary layer thickness). The instantaneous wall-normal velocity fluctuation is modeled as the negative of the last addend in the construction leading to u:

$$w = -a_{N_z}. \tag{6}$$

This last step ensures a negative correlation so that the mean momentum flux is constant in the log region:

$$\langle uw\rangle = \sum_{i=1}^{N_z}\langle a_i a_{N_z}\rangle = -\langle a_{N_z}^2\rangle = -\langle a^2\rangle. \tag{7}$$

A notional attached eddy is sketched in Fig. 2 and a top view of the modeled flow field is sketched in Fig. 3. By relating a_i with an attached eddy of height $\delta/2^i$, we have discretized the boundary layer logarithmically in the wall-normal direction. The base 2 is arbitrary but convenient and is chosen for consistency with Ref. [37]. We now make an additional geometric assumption about the aspect ratio of the wall-attached eddies. We assume that wall-attached eddies at a height h may be characterized by lengths l_x and l_y in the streamwise and spanwise directions, respectively. Therefore, an attached eddy of height h affects two points which lie nominally within the $l_x \times l_y$ area of influence (cf. Fig. 2). Let us further denote the aspect ratio $R = l_y/l_x$ as a given, z-independent geometric constant (for empirical evidence for geometric self-similarity in the logarithmic region, see, e.g., recent detailed analyses of DNS by del Álamo *et al.* [38]). In other words, two points such that $z < h$, $z + r_z < h$,

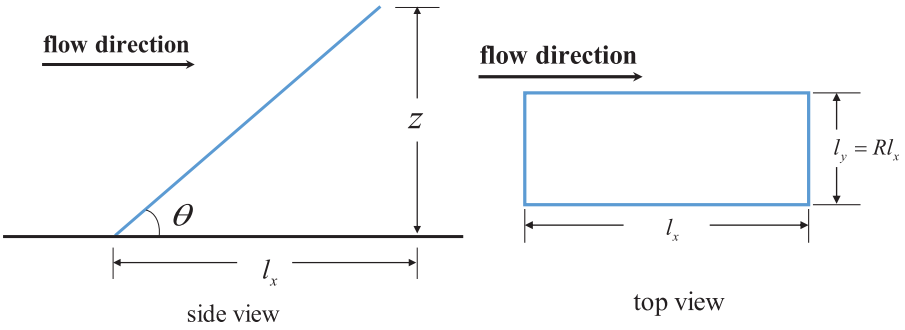

FIG. 2. Conceptual sketch of a notional attached eddy of height z. This eddy extends and affects an area of $l_x \times l_y$ (in $x \times y$ plane). The inclination angle of this eddy is θ. $l_x = z/\tan(\theta)$. Define $R = l_y/l_x$ to be the aspect ratio, it follows that $l_y = Rz/\tan(\theta)$. Because of the assumed similarity, R, θ are z-independent geometric constants.

$r_x < h/\tan(\theta)$, $r_y < Rh/\tan(\theta)$ share all addends from eddies of height greater than h. Such a compact representation of eddy-induced velocity fluctuations allows us to make predictions on the scalings of various flow statistics in the logarithmic region, where the eddies are self-similar, and the random addends a_i are statistically identical, as are the addends b_i (see Refs. [23,39] for detailed discussion).

We assume that large-scale eddies do not directly interact with small-scale eddies, and that a_i, a_j, $i \neq j$ are statistically independent (so are b_i, b_j, $i \neq j$). a_i and b_i are therefore independent random variables, each of which are identically distributed (but a_i and b_i possibly have different distributions). Neglecting interscale interactions (or interactions among different heights) must be here considered as a first approximation. Amplitude modulation effects [40,41] observed in the vicinity of the wall have not yet been explored in detail among scales and eddies in the log region. To the degree that they occur, these can be considered as a higher-order corrections to the simplest approximation made here of assuming independence. Furthermore, amplitude modulation is an important process for odd-order statistics, but for second-order statistics, accounting for the effects of modulation or not does not make a significant difference [42]. At a distance z from the wall, the influence of an attached eddy of size $\ll z$ becomes negligible, and therefore the number of random addends in Eq. (5) can simply be obtained by integrating the eddy population density $P(z) \sim 1/z$

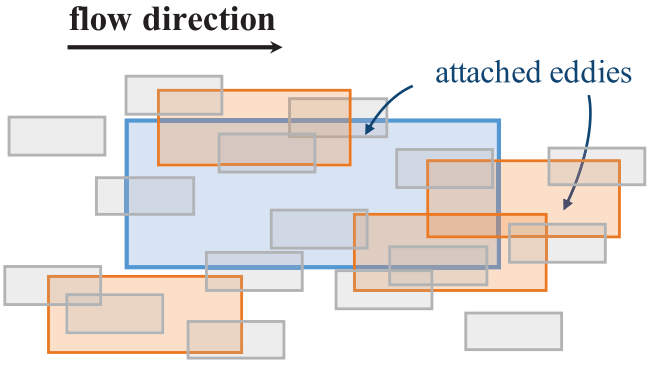

FIG. 3. Top view of the modeled wall-bounded flow showing a random superposition of notional wall attached eddies. Wall eddies tend to be stretched in the flow direction. Because eddy population density is inversely proportional to the wall-normal distance, the number of observable eddies on an x-y plane quadruples as the sizes of the eddies halve. Wall-attached eddies of different sizes are colored differently.

from z to δ, leading to

$$N_z \sim \int_z^\delta P(z) \sim \log(\delta/z). \tag{8}$$

As an example of possible applications of the HRAP model, we compute $\langle u^2\rangle$, $\langle v^2\rangle$. Squaring both sides of Eq. (5) leads to

$$\begin{aligned}\langle u^2\rangle &= N_z\langle a^2\rangle \sim \log(\delta/z) = A_1\log(\delta/z) + B_1,\\ \langle v^2\rangle &= N_z\langle b^2\rangle \sim \log(\delta/z) = A_{1,v}\log(\delta/z) + B_{1,v},\end{aligned} \tag{9}$$

recovering the logarithmic scaling for $\langle u_z^2\rangle$ and $\langle v_z^2\rangle$. Here, A_1, $A_{1,v}$, B_1, and $B_{1,v}$ are constants. The value of A_1, the Townsend-Perry constant, has been determined empirically, yielding $A_1 \approx 1.2$–1.3 [36]. In this work, Eqs. (5), (6), and (8) are used to provide estimates for all scalar functions in Eq. (2).

III. SCALING OF GENERAL TWO-POINT STRUCTURE FUNCTIONS

We begin by defining the "associated eddy height" corresponding to particular (specified) horizontal displacements r_x and, separately, r_y. Specifically, we define

$$z_{rx} = |r_x|\tan(\theta), \quad z_{ry} = \frac{|r_y|}{R}\tan(\theta). \tag{10}$$

The height z_{rx} is the minimum height of an eddy that can simultaneously affect two points with a displacement r_x only in the streamwise direction. In other words, two points separated by a distance r_x can be affected only by an eddy with a height greater than z_{rx}. Similarly, for displacements only in the transverse direction r_y, z_{ry} is the height corresponding to an eddy of x-direction length r_y/R. For now we are assuming these two heights are smaller than δ. For arbitrary displacements r_x and r_y, we define

$$z_c = \min\{\max[|r_x|,|r_y|/R]\tan(\theta),\delta\}, \tag{11}$$

which is the minimum height of an eddy that simultaneously affects two points at a distance r_x, r_y in the x, y directions, given that the boundary layer can not admit eddies higher than δ. We assume that the displacements are larger than a minimum value so that the velocity fluctuations at the two points differ at least by one addend. For smaller displacements, the two-points are considered equivalent in the framework of HRAP, and the associated structure function follows the inertial-range scalings.

Applying the HRAP model to determine $D_{11}(r_x,r_y,r_z,z)$, we must determine the number of common addends shared by the two points. For this purpose we focus on the vertical location of the higher point, at $z+r_z$ ($r_z>0$). Depending on r_x and r_y, we can identify three regimes (see Fig. 4):

$$\mathrm{I}: z_c < z+r_z, \quad \mathrm{II}: z+r_z < z_c < \delta, \quad \mathrm{III}: z_c = \delta. \tag{12}$$

For two points in regime III, the points share no common eddy, hence

$$\begin{aligned}D_{11} &= \left\langle\left(\sum_{i=1}^{N_z} a_i' - \sum_{i=1}^{N_{z+r_z}} a_i''\right)^2\right\rangle = \left(N_z + N_{z+r_z}\right)\langle a^2\rangle - 2\left\langle\left(\sum_{i=1}^{N_z} a_i'\right)\cdot\left(\sum_{i=1}^{N_{z+r_z}} a_i''\right)\right\rangle\\ &= \left(N_z + N_{z+r_z}\right)\langle a^2\rangle = A_1\log\left(\frac{\delta}{z}\right) + A_1\log\left(\frac{\delta}{z+r_z}\right) + C_3.\end{aligned} \tag{13}$$

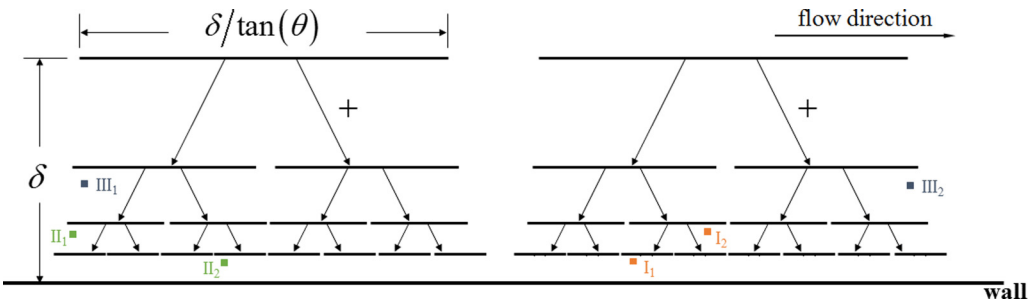

FIG. 4. Examples of pairs of points in regimes I, II, and III. For two points in regime III (indicated as points III_1, III_2), III_1 shares none of its addends with III_2. For two points in regime I (indicated as points I_1, I_2), I_1 share all common addends with I_2 (and then I_1 includes an extra addend since it is closer to the wall). For two points in regime II (II_1, II_2), II_1 share part of the addends with II_2 (specifically in this example, addends from eddies of height δ, $\delta/2$). The schematic is in accordance with Fig. 1. As is sketched in Fig. 1, a horizontal line corresponds to an eddy and affects the region below it. While the sketch is artificially regular for purposes of illustration, in reality the model encompasses more random spatial arrangements of eddies as in Fig. 3.

For two points in regime I, point $\mathbf{x}$ share all the eddies that affect $\mathbf{x}+\mathbf{r}$ ($0 < r_z$), hence

$$D_{11} = \left\langle \left[\left(\sum_{i=1}^{N_{z+r_z}} a_i + \sum_{i=N_{z+r_z}}^{N_z} a_i' \right) - \left(\sum_{i=1}^{N_{z+r_z}} a_i \right) \right]^2 \right\rangle$$
$$= \left\langle \left[\sum_{i=N_{z+r_z}}^{N_z} a_i' \right]^2 \right\rangle = \left(N_z - N_{z+r_z}\right)\langle a^2 \rangle = A_1 \log\left(\frac{z+r_z}{z}\right) + C_1. \tag{14}$$

Note that we are excluding from these considerations the transition towards the locally isotropic scaling that occurs when $r = (r_x^2 + r_y^2 + r_z^2)^{1/2} < C_z z$, where C_z is an $O(1)$ constant. For regime I, typically r_x and r_y are small and therefore we must limit r_z to be (typically) larger than z. Thus the scaling implied by Eq. (14) is meant to hold for $r_z/z \gtrsim 1$. In the limit $r_z/z \lesssim 1$, a transition towards the inertial range scaling is envisioned.

For two points in regime II, points (x,y,z) and $(x+r_x, y+r_y, z+r_z)$ share the eddies of height greater than z_c, hence

$$D_{11} = \left\langle \left[\left(\sum_{i=1}^{N_{z_c}} a_i + \sum_{i=N_{z_c}}^{N_z} a_i' \right) - \left(\sum_{i=1}^{N_{z_c}} a_i + \sum_{i=N_{z_c}}^{N_{z+r_z}} a_i'' \right) \right]^2 \right\rangle = \left\langle \left[\sum_{i=N_{z_c}}^{N_z} a_i' - \sum_{i=N_{z_c}}^{N_{z+r_z}} a_i'' \right]^2 \right\rangle$$
$$= \left(N_z - N_{z_c}\right)\langle a^2 \rangle + \left(N_{z+r_z} - N_{z_c}\right)\langle a^2 \rangle - 2\left\langle \left(\sum_{i=N_{z_c}}^{N_z} a_i' \right) \cdot \left(\sum_{i=N_{z_c}}^{N_{z+r_z}} a_i'' \right) \right\rangle$$
$$= \left(N_z - N_{z_c}\right)\langle a^2 \rangle + \left(N_{z+r_z} - N_{z_c}\right)\langle a^2 \rangle = A_1 \log\left(\frac{z_c}{z}\right) + A_1 \log\left(\frac{z_c}{z+r_z}\right) + C_2, \tag{15}$$

where a, a', a'' are i.i.d. variables. Imposing continuity of D_{11} with respect to z_c, it is clear that the constants C_1, C_2, C_3 must be equal,

$$C_1 = C_2 = C_3. \tag{16}$$

It is worth noting that, although we have discretized the log region into discrete hierarchical scales and both N_z, N_{z+r_z} are integers that take only discrete values, because in Eq. (8) the integration is a continuous function of z, the predictions here are continuous functions of z and $\mathbf{r}$. Combining

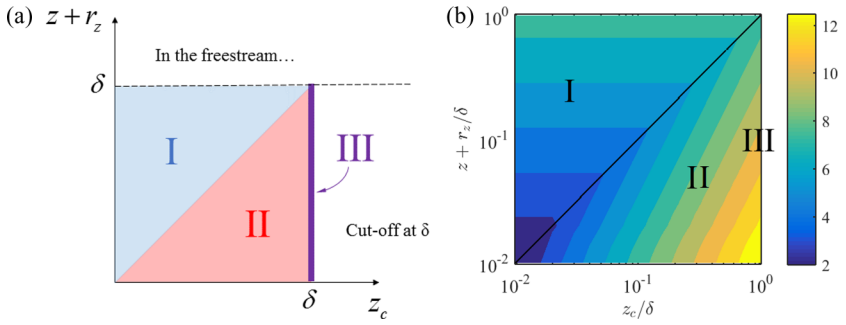

FIG. 5. (a) A sketch of the various regimes used to evaluate the scaling of D_{11} under the HRAP simplified attached eddy model. The definition of z_c is cut off at δ, therefore regime III is indicated only at $z_c = \delta$. $z + r_z$ is required to be in the boundary layer, i.e., $z + r_z < \delta$. (b) Contour levels computed according to Eq. (18) for D_{11} as a function of z_c and $z + r_z$ for $z = 0.01\delta$, using $A_1 = 1.25$ and setting $C_{11} = 2$ for purposes of illustration.

Eqs. (12)–(16), we have

$$\begin{aligned} D_{11} &= A_1 \log\left(\frac{z+r_z}{z}\right) + C_{11}, \quad z_c < z + r_z, \\ D_{11} &= A_1 \log\left(\frac{z_c}{z}\right) + A_1 \log\left(\frac{z_c}{z+r_z}\right) + C_{11}, \quad z + r_z < z_c < \delta, \\ D_{11} &= A_1 \log\left(\frac{\delta}{z}\right) + A_1 \log\left(\frac{\delta}{z+r_z}\right) + C_{11}, \quad z_c = \delta, \end{aligned} \tag{17}$$

where C_{11} is a constant. Defining $z_e = \max[z_c, z + r_z]$, a compact form of D_{11} is

$$D_{11} = A_1 \log\left(\frac{z_e}{z}\right) + A_1 \log\left(\frac{z_e}{z+r_z}\right) + C_{11}, \tag{18}$$

where we recall that z and $z + r_z$ are assumed to fall in the logarithmic layer, i.e., significantly below δ.

The various regimes are sketched in Fig. 5(a). Essentially we seek the minimum height h_c of an eddy that can simultaneously affect the two points under consideration. Because of the treelike organization of the attached eddies, the effects of eddies with height $h > h_c$ is canceled (because we are taking the difference between the two points when evaluating structure functions). Effects of eddies of heights $h < h_c$ remain and are reflected separately on two points, in the form

$$\log\left(\frac{h_c}{z}\right) + \log\left(\frac{h_c}{z+r_z}\right). \tag{19}$$

It is useful to point out that h_c is not necessarily equal to z_c since z_c is the minimum height of an eddy that could affect two points with a displacement r_x, r_y in the x, y directions. The two points could be displaced by a very small distance in the x-y plane but by a large distance in the vertical direction. In that case, h_c becomes $z + r_z$ and we are in regime I. Regime II is straightforward, where $z_c = h_c$. If the two points are so separated that to affect them simultaneously one needs an eddy of height greater than δ, then we are in regime III. The description stops at $z_c = h_c = \delta$ (since the boundary layer does not admit any eddy whose height is greater than δ). A sketch of D_{11} as a function of z_c and $z + r_z$ is shown in Fig. 5(b). The contour levels are computed according to Eq. (18). The hidden parameter z is 0.01δ, which is chosen arbitrarily for illustration purposes.

A few asymptotes of Eq. (17) have been investigated previously. For example, taking $r_z = 0$ and $r_x \gg \delta$ (and/or $r_y \gg \delta$), we have $z_c = \delta$, $z_e = \delta$ and we obtain $D_{11} = 2A_1 \log(\delta/z) + C_{11}$, i.e., the logarithmic scaling of $\langle u^2 \rangle = \frac{1}{2} D_{11}(|\mathbf{r}| \gg \delta, z)$ as a function of z is recovered. Taking $r_z = r_y = 0$

and r_x in the relevant range [an r_x such that $r_x > z$ but a converted wall-normal height $r_x \tan(\theta)$ still in the log region], we have $z_c \sim r_x$, $z_e = z_c \sim r_x$ and the scaling $\langle [u(x+r_x) - u(x)]^2 \rangle = 2A_1 \log(r_x/z) + C$ is obtained [20].

New scaling laws can be obtained from Eq. (17), e.g., taking $r_x = 0$, $r_z = 0$ and r_y in the range such that $r_y \gtrsim z$ and the corresponding wall-normal height $r_y/R \cdot \tan(\theta)$ in the log region, we have $z_c \sim r_y$, $z_e = z_c \sim r_y$ and thus

$$\langle [u(x,y,z) - u(x,y+r_y,z)]^2 \rangle \sim 2A_1 \log(r_y/z), \tag{20}$$

i.e., a transversal logarithmic scaling similar to the longitudinal one found in de Silva *et al.* [20]. According to the HRAP model, the transverse scaling has the same slope $2A_1$ as the longitudinal one, because geometric parameters including R, $\tan(\theta)$ that enter z_c, z_e can be absorbed into the additive constants without affecting the slope. Or, taking $r_x = 0$, $r_y = 0$, r_z in the range such that $z + r_z$ is still in the logarithmic region, we have $z_c = z + r_z$, $z_e = z_c = z + r_z$ and thus

$$\langle [u(x,y,z+r_z) - u(x,y,z)]^2 \rangle \sim A_1 \log[(z+r_z)/z], \tag{21}$$

now with slope A_1 instead of $2A_1$, predictions that should be interesting to confirm based on data.

Next the HRAP model can be applied for D_{22}. According to Eq. (5), both u, v are results of additive processes, the only difference is that for v the addends b_i may have different statistics to those of a_i. Hence, the scaling behavior of D_{22} is similar to those of D_{11} but involving $\langle b^2 \rangle$ instead of $\langle a^2 \rangle$. Thus, we obtain

$$D_{22} = A_{1,v} \log\left(\frac{z_e}{z}\right) + A_{1,v} \log\left(\frac{z_e}{z+r_z}\right) + C_{22}, \tag{22}$$

where $A_{1,v}$, C_{22} are constants. Similar scalings including $\langle [v(x,y,z) - v(x,y+r_y,z)]^2 \rangle \sim 2A_{1,v} \log[r_y/z]$, $\langle (v_{z+r_z} - v_z)^2 \rangle \sim A_{1,v} \log[(z+r_z)/z]$ are expected as well. Again the prefactors of the streamwise and transverse logarithmic scalings are the same, but offset constants are possibly different.

The last diagonal term D_{33} is considered next:

$$\begin{aligned} D_{33} &= \langle [w(x+r_x,y+r_y,z+r_z) - w(x,y,z)]^2 \rangle \\ &= 2\langle ww \rangle - 2\langle w(x+r_x,y+r_y,z+r_z) w(x,y,z) \rangle. \end{aligned} \tag{23}$$

We have assumed that the streamwise velocity fluctuations at the two points differ at least by one addend (if not, then the structure function follows the inertial range scalings), therefore the last addend in $u(x,y,z)$, which controls the wall-normal component $w(x,y,z)$, is statistically independent of the last addend in $u(x+r_x,y+r_y,z+r_z)$, which controls the wall-normal component $w(x+r_x,y+r_y,z+r_z)$. Let us use a for the addends in $u(x,y,z)$ and a' for the addends in $u(x+r_x,y+r_y,z+r_z)$. We have $\langle w(x+r_x,y+r_y,z+r_z) w(x,y,z) \rangle = \langle a_{N_z} a'_{N_{z+r_z}} \rangle = 0$, and therefore

$$D_{33} = 2. \tag{24}$$

We have made the approximation that $\langle ww \rangle = 1$ in the log region. That is to say, the normal vertical velocity structure function transitions from the inertial regime to a constant value ($\sim$2) for displacements larger than the height above the wall. Because the HRAP model predicts a constant value for D_{33} in the logarithmic region, Eq. (24) does not provide a length scale for the D_{33} scaling and because $D_{33} \equiv 2$ in the logarithmic region, D_{33} should collapse by plotting against r_x/δ and r/z, at least in the logarithmic range. Therefore the collapse of D_{33} scaling depends on the r_x range within which a transition from the inertial range scaling to the logarithmic range scaling takes place. Because this transition occurs at around $r \sim O(z)$, the length scale for constant scalings like the one in Eq. (24) should be z and we expect a collapse of data when D_{33} is plotted as a function of r/z.

Eqs. (18), (22), and (24) summarize the scaling behaviors of all three diagonal components of D_{ij}. Next, the off-diagonal components are evaluated. Given a_i, b_i are independent variables, we

can immediately conclude

$$D_{12} = 0, \quad D_{23} = 0, \tag{25}$$

also consistent with the requirement of reflectional symmetry. The last term to be evaluated is the shear term, D_{13}:

$$D_{13} = \langle [u(\mathbf{x}+\mathbf{r}) - u(\mathbf{x})][w(\mathbf{x}+\mathbf{r}) - w(\mathbf{x})] \rangle = 2\langle uw \rangle - \langle u(\mathbf{x}+\mathbf{r})w(\mathbf{x}) \rangle - \langle u(\mathbf{x})w(\mathbf{x}+\mathbf{r}) \rangle. \tag{26}$$

The first term $\langle uw \rangle = -u_\tau^2 = -1$. Let us consider the two cross terms. Without loss of generality, we have assumed $r_z \geqslant 0$. Then $z + r_z \geqslant z$ and $N_{z+r_z} \leqslant N_z$. $\langle u(\mathbf{x}+\mathbf{r})w(\mathbf{x}) \rangle = -\langle \sum_{i=1}^{N_{z+r_z}} a_i' \cdot a_{N_z} \rangle$ is directly 0 for $N_{z+r_z} < N_z$ because addends with different indices are statistically independent; for $N_{z+r_z} = N_z$, $\langle u(\mathbf{x}+\mathbf{r})w(\mathbf{x}) \rangle$ is $-\langle a_{N_z} a_{N_z}' \rangle$, which is also 0 because the streamwise velocity fluctuations at the two points differ at least by one addend (otherwise the structure function just follow the inertial range scalings). Now let us consider the other cross term $\langle u(\mathbf{x})w(\mathbf{x}+\mathbf{r}) \rangle$. Again because addends for eddies of different sizes are uncorrelated and because $N_z \geqslant N_{z+r_z}$, $\langle u(\mathbf{x})w(\mathbf{x}+\mathbf{r}) \rangle = -\langle \sum_{i=1}^{N_z} a_i \cdot a_{N_{z+r_z}}' \rangle = -\langle a_{N_{z+r_z}} a_{N_{z+r_z}}' \rangle$. For two points in regimes II, III, this cross term vanishes because the size of the smallest common eddy is greater than $z + r_z$ and $a_{N_{z+r_z}}, a_{N_{z+r_z}}$ are statistically independent. For two points in regime I, $a_{N_z} = a_{N_z}'$ and the cross term $\langle u(\mathbf{x})w(\mathbf{x}+\mathbf{r}) \rangle$ is -1. Hence, for the range of $\mathbf{r}$,$\mathbf{x}$ discussed in this work:

$$D_{13} = -1 \quad z_c < z + r_z, \quad D_{13} = -2 \quad z + r_z < z_c. \tag{27}$$

The discontinuity is because the assumed region of influence of an attached eddy is not a well-behaved function that decays smoothly to 0, but instead is a function that jumps to 0.

Equations (18), (22), (24), (25), and (27) are the complete description of the scalings of the structure function in the logarithmic region. It is worth noting that the $-2/3$ power-law scaling in the inertial range is not incorporated up to this point but smooth transitioning to power-law inertial range scaling is expected whenever $\sqrt{r_x^2 + r_y^2 + r_z^2} < C_z z$, where C_z is a constant of $O(1)$.

Note that in the model the assumed eddy inclination angle θ and the eddy aspect ratio R do not appear explicitly in the scaling law. These parameters do enter, however, when determining the limits between the various scaling regimes. For instance, the eddy inclination angle is used to compute a streamwise extent within which an attached eddy of height h exerts its influence on, while the aspect ratio R affects the scaling limits when considering various r_y and r_x combinations. We remark further that for more realistic modeling of wall-bounded flows, an eddy tilting angle might also be used to account for the lag of the effects of attached eddies across the wall-normal direction (see, e.g., Ref. [41] for discussion of this effect). Last, the assumption of a_i, b_i being i.i.d. variables may not hold exactly. However, in the high Reynolds number limit, the variance $\langle u^2 \rangle \sim \log(\delta/z)$ does not strictly require i.i.d. but rather holds provided correlations have sufficiently rapid decay (the logarithmic scaling of cumulants is indicative of a large deviations principle [43,44] and is not restricted to i.i.d. variables [2]). Similarly, $\langle uw \rangle = -1$ is constant according to the HRAP model but is in fact only approximately so in the log region for finite Reynolds number, indicating already the z dependence of the random addends. Because of this wall-normal dependence at finite Reynolds number, scalings including $\langle u^2 \rangle = a_1^2 + a_2^2 + \cdots + a_{N_z}^2$ are only approximately $\log(\delta/z)$, and deviations from the log scaling are expected to be similar to the deviations of $\langle uw \rangle$ from a constant -1. It should be kept in mind that the attached eddy hypothesis and the HRAP model used here are models for the high Reynolds number limit and are therefore only approximate for any finite Reynolds number.

IV. EMPIRICAL EVIDENCE FOR PROPOSED SCALINGS

Statistics that involve streamwise displacements can be evaluated from a single hot-wire measurement by invoking Taylor's hypothesis [28,45,46]. Evaluating statistics that include a displacement in the spanwise direction requires much more work in a laboratory experiment because it needs simultaneous measurements at multiple spanwise locations. It is possible to resort

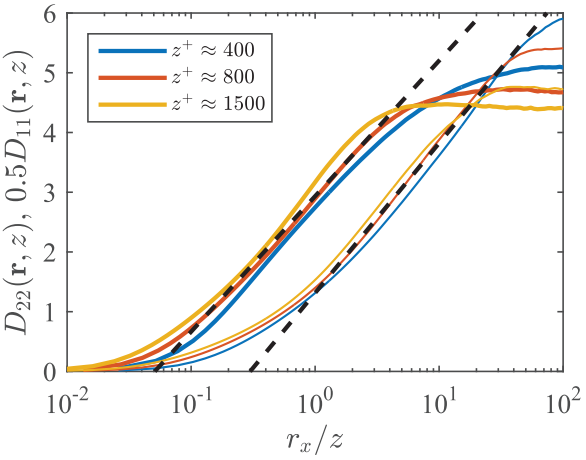

FIG. 6. Linear-log plot of $D_{22}(r_x,0,0;z)$ and $0.5D_{11}(r_x,0,0;z)$ as functions of r_x measured experimentally at $\mathrm{Re}_\tau \approx 15\,000$ at wall-normal locations $z^+ = 400$, 800, 1500. The thin lines are for D_{11} and the bold lines are for D_{22}. The straight dashed lines indicate the fitted slopes of the logarithmic scalings.

to numerical simulations for such measurements, but for numerical simulations, direct numerical simulations (DNS) in particular, the limited Reynolds number is an obstacle. The highest Reynolds number accomplished to date for a channel flow using DNS is $\mathrm{Re}_\tau \approx 5000$ [18]. The reader is directed to Refs. [47–52] for more DNS data sets of turbulent channel flows. In this section, the streamwise scalings, D_{ij} as functions of $r = (r_x,0,0)$ are investigated using hot-wire measurements in boundary layer flows. Spanwise scalings and trends in other directions, on the other hand, are examined using channel flow DNS data sets.

Recent work [53] suggested applying extended-self-similarity (ESS) to structure functions to obtain scaling behavior of improved quality, following the success of ESS in the context of moment-generating functions [54]. ESS is useful when considering scalings of higher-order moments relative to the scaling of a known lower-order moment. Here we consider only the second-order statistics and we require scaling ranges for different physical quantities in different directions (spanwise, vertical), therefore the usefulness of ESS in the present context is not immediately clear.

To document the streamwise logarithmic scalings, we use the cross-wire measurements taken in boundary layer flows at $\mathrm{Re}_\tau \approx 15000$ (where u,w components are measured in one experiment and u,v components are measured in another experiment). Details of the experimental setup can be found in Refs. [17,55] and the references cited therein. The sampling frequency is high enough to allow streamwise displacements smaller than $r_x^+ = 10$, which falls much below the range of two-point displacement of interest ($r^+ \gtrsim z^+ \gg 100$). The use of Taylor's hypothesis for quantities such as structure functions is common and has been proven to be valid [20,56]. The streamwise logarithmic scaling for D_{11} was confirmed in Ref. [20] and can be observed in Fig. 6, where $0.5D_{11}$ is shown as a function of r_x at wall-normal heights $z^+ \approx 400,800,1500$. The prefactor 0.5 is used for better visualization when plotted together with D_{22}, which is also shown in Fig. 6. The figure shows D_{22} as functions of r_x/z at three wall-normal locations. The data collapse when plotted against r_x/z. Because of the high Reynolds number, a logarithmic region that spans more than a decade is found both in D_{11} and D_{22} in the streamwise direction. The slope for D_{11} is fitted here in the r_x range $1 < r_x/z < 10$, and the fitted slope results in 2.2, not far from prior measurements where $2A_1 = 2.5$. As for the slope of the streamwise logarithmic scaling of D_{22}, the fitted slope is 0.99. This is very close to the expected slope of $2A_{1,v}$, where $A_{1,v} \approx 0.5$ is the slope of $\langle v^2 \rangle$ (as a function of z) measured previously [17,51]. Compared to D_{11}, one notes that the logarithmic scaling region for D_{22} occurs at smaller scales as the curves appear to be shifted to the left, by almost a factor 6. This means that C_{22} is considerably higher than C_{11}, which is consistent with effects

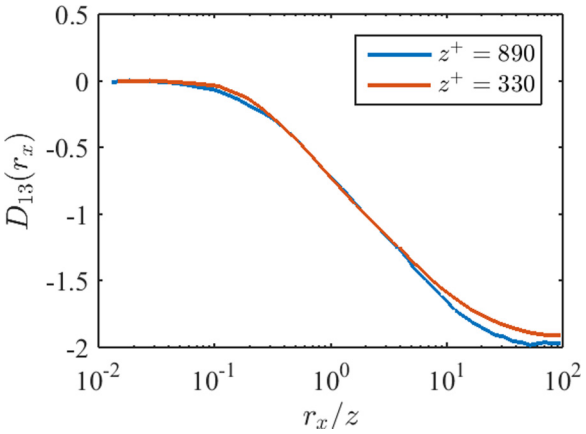

FIG. 7. Linear-log plot of $D_{13}(r_x,0,0,z)$ at $\mathrm{Re}_\tau \approx 15\,000$ as a function of r_x at two wall-normal heights.

from the continuity equation that leads to smaller integral length scales for transverse correlations as compared to longitudinal ones. A factor 6, however, is quite large.

By symmetry one expects $D_{12} \equiv 0$, which is also predicted by the HRAP. The experimental hot-wire results (not shown) are consistent with low values of D_{12} (the data are slightly negative, $D_{12} \approx -0.1$ in wall units, at large streamwise displacements possibly due to small misalignments of the cross-wires and possible uncertainties in the measurements).

Figure 7 shows D_{13} as a function of r_x at two wall-normal locations. D_{13} collapse when plotted against r_x/z. For sufficiently large two-point displacement r_x, $D_{13} = -2$, as suggested by the HRAP model and required by the fact that the mixed structure function must asymptote to twice (negative) the square of the friction velocity at large distances. For $r_x \lesssim z$, the structure functions should follow the inertial range scalings and such scalings were discussed in Refs. [33,34]. Note for two points that are displaced only in the streamwise direction, we never actually enter regime I.

Figure 8 shows $D_{33} - 2\langle w^2\rangle$ as functions of r_x/z. The data do not collapse when D_{33} itself is plotted as a function of r_x/z at different wall-normal locations (not shown), but by subtracting $\lim_{r_x\leftarrow\infty} D_{33} = 2\langle w^2\rangle$ from D_{33}, a good collapse is found, as is seen in Fig. 8. This suggests that the difference in D_{33} is from fine-scale motions in the regime $r_x \lesssim z$ [57,58]. Beyond $r_x \approx z$, D_{33} tends to $2\langle w^2\rangle$, consistent with the model although the exact magnitude of $\langle w^2\rangle$ is not 1 in wall

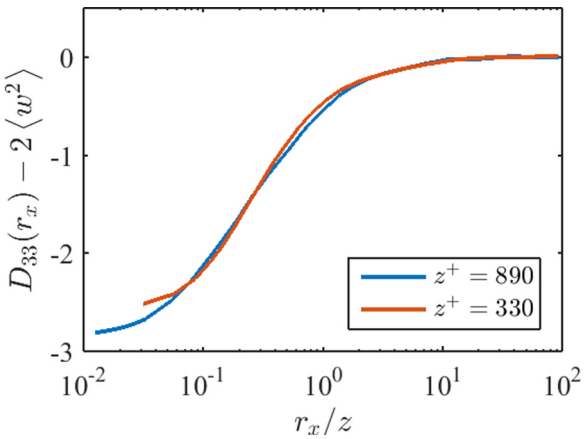

FIG. 8. Linear-log plot of $D_{33}(r_x,0,0,z)$ at $\mathrm{Re}_\tau \approx 15\,000$ as a function of r_x at two wall-normal locations $2\langle w^2\rangle$ at the two wall-normal locations are 2.5 and 2.8, respectively.

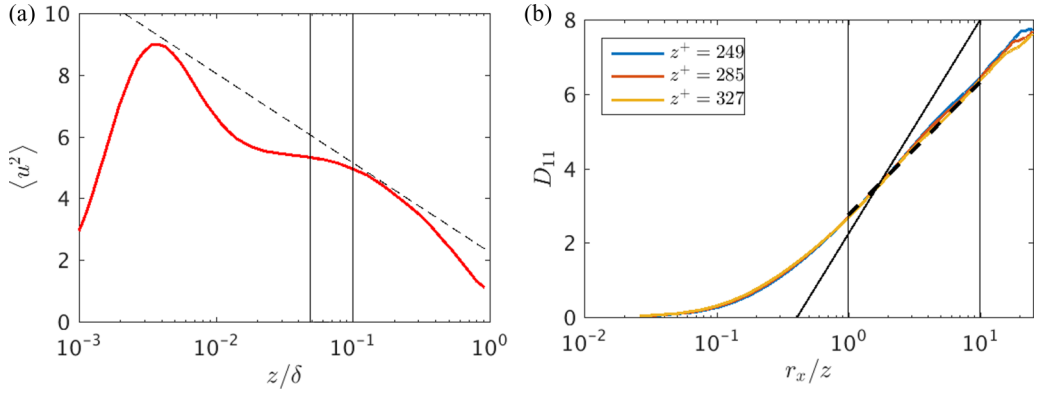

FIG. 9. (a) Streamwise variance $\langle u^2 \rangle$ as a function of the wall-normal distance for the $\mathrm{Re}_\tau \approx 4200$ DNS. The dashed line has a slope 1.26. The two vertical lines enclose the expected log region and are at $z^+ = 3\sqrt{Re_\tau}$ and $z/\delta = 0.1$. (b) $D_{11}(r_x,0,0,z)$ plotted against r_x at three wall-normal distances within the enclosed region in (a). A log region is found in the enclosed region. The fitted slope within the enclosed region is 1.6 and is indicated using a dashed line. The expected slope is ≈2.5 and is indicated using a thin solid line.

units. The transition from the inertial range scalings to the logarithmic range scalings occurs near $r_x/z \sim O(0.1)$. Note that scalings in the logarithmic range are not necessarily log scalings, e.g., the scaling of D_{33} in the logarithmic range is a constant scaling -2 instead of a logarithmic scaling. Comparing D_{33} and D_{13}, the transitions to log-range scalings are at quite different r_x/z distances, with D_{33} transitioning at smaller distances than D_{13}. This difference is not surprising if one considers first the fact that w is controlled mostly by a local eddy while u is affected by larger eddies, and second the aforementioned difference in the integral scales between the transverse and longitudinal components.

For empirical evidence of the spanwise scalings, we require simultaneous measurements at a number of spanwise distances. For this purpose we use the $\mathrm{Re}_\tau = 4200$ DNS channel-flow dataset [51]. The DNS has used a grid of size $3072 \times 3072 \times 1081$ (in x, y, z directions) for a computational domain of size $2\pi \times \pi \times 2$, where the half channel height is 1.

Figure 9(a) shows $\langle u^2 \rangle$ as a function of the wall-normal distance. In Fig. 9(b), we show $D_{11}(r_x,0,0;z)$ as a function of r_x at different wall-normal locations. As seen in Fig. 9, although no logarithmic region can be found in $\langle u^2 \rangle$ as a function of z, a logarithmic region can be discerned in the streamwise velocity structure function as a function of r_x. Nevertheless, the measured slope is 1.6, whereas at high Reynolds numbers, the observed slope is $2A_1 \approx 2.5$. Thus even if a logarithmic scaling is observed, one may expect differences of at least 40% when comparing with values expected at high Reynolds numbers. This insight will be useful when measuring scaling parameters in directions where only DNS data are available. In terms of the behavior at sufficiently large r_x, at which $\langle u(x)u(x+r) \rangle = 0$, we expect $D_{11} = 2\langle u^2 \rangle$. For the current dataset, the two-point correlation at $r = L_x/2$, where L_x is the streamwise dimension of the periodic computational domain, does not drop to 0 due to the limited size of the channel. As a result, D_{11} does not reach $2\langle u^2 \rangle$ in Fig. 9(b) at large r_x values.

Figure 10 shows D_{11}, D_{22} as functions of the spanwise displacement r_y at three wall-normal heights $z^+ \approx 249, 285, 327$. The data are obtained by averaging over one snapshot of the DNS, so at large r_y some fluctuations are visible due to lack of convergence. Nevertheless, logarithmic scalings are observed within the region indicated by the vertical lines. Such behavior is consistent with the HRAP model. While the streamwise velocity correlation does not drop to 0 at $r_x = L_x/2$, the correlation in the spanwise direction decays to 0 at $r_y = L_y/2$, where L_y is the spanwise dimension of the computational domain. As a result, at sufficiently large r_y, both D_{11} and D_{22} tend to $2\langle u^2 \rangle$ [which can be confirmed by comparing Figs. 10(a) and 9(a)] and $2\langle v^2 \rangle$ (not shown).

The measured slope for $D_{11}(r_y)$ and $D_{22}(r_y)$ are, respectively, 3.7 and 1.3. According to HRAP, the expected slopes for the spanwise logarithmic scalings should be the same as their streamwise

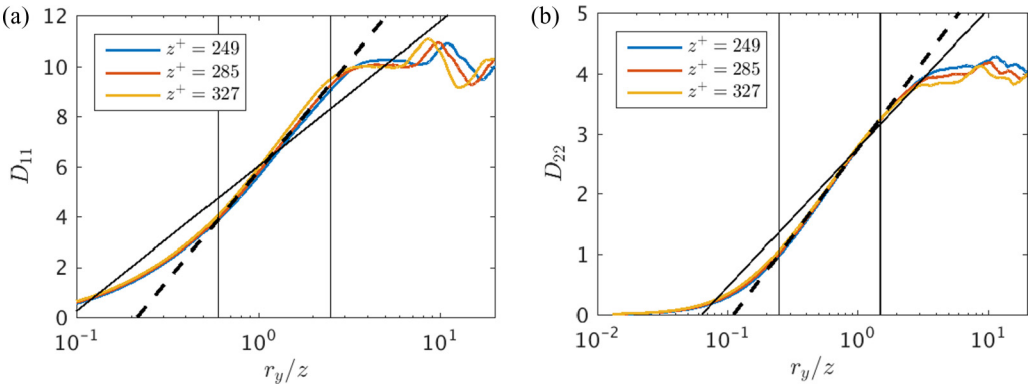

FIG. 10. Linear-log plot of $D_{11}(0,r_y,0;z)$, $D_{22}(0,r_y,0;z)$ as function of r_y at three wall-normal heights $z^+ \approx 249,285,327$. The measured slopes are 3.7, 1.3 for D_{11} and D_{22} and are shown using dashed lines. The expected slopes ($2A_1 = 2.5$ and $2A_{1,v} = 1.0$) are indicated using thin solid lines.

counterparts, which at high Reynolds numbers are ∼2.5 and ∼1.0, respectively. The difference between the measured and expected slopes is on the order of 30%–40%. However, we note that it is a difference in the opposite direction as that noted before: for r_y the DNS is showing larger slopes than the expected high Reynolds number scaling, whereas it gave lower values for the streamwise displacement, r_x scaling. The difference between the measured slope and the expected slope could be due to a few reasons: first, as was mentioned above, the limited Reynolds number of the data, because of which, a log region is absent in $\langle u^2 \rangle$ and hence any expectations based on the slope of $\langle u^2 \rangle$ would also be not observable from the data [59]; second, the difference between large-scale fluid motions in channel flow and boundary layer flow, the former of which lacks a second very long mode in the premultiplied spectrum when compared to channel flow [56]; and third, the limited size the computational domain [51], etc. It may also be that the slopes should indeed be different from the expected ones according to the HRAP model because of physical processes that are not accounted for here. For now, we simply remark that data at higher Reynolds numbers are needed to provide more definitive confirmation or refutation of the HRAP prediction that the slopes in r_y should be equal to those in the r_x direction.

Next we examine trends and scalings with wall-normal displacements, where $\mathbf{r} = (0,0,r_z)$. For two points that are displaced in the wall-normal direction, D_{11} and D_{22} follow the scalings $D_{11}(0,0,r_z;z) \sim A_1 \log[(z+r_z)/z]$, $D_{22}(0,0,r_z;z) \sim A_{1,v} \log[(z+r_z)/z]$ (see earlier discussion in Sec. III). Thus we may examine the scaling by plotting as a function of $\log(z+r_z)$ for fixed z, or by fixing $z+r_z$ and plotting as a function of $\log(z)$. Since we must ensure that $z+r_z$ is limited to below δ, the latter is more natural. Figure 11 shows $D_{11}(0,0,r_z;z)$, $D_{22}(0,0,r_z;z)$ as functions of z for a specified $z+r_z$ value (we choose $z+r_z = 0.4\delta$). The results are marked as "not displaced." For D_{11} a possible scaling range appears to form above $z^+ \sim 300$ with a slope that is consistent with the prediction from HRAP (which is $A_1 \approx 1.25$ for D_{11}). For D_{22} a longer range appears starting around $z^+ \sim 50$, and a slope consistent with $A_{1,v} \approx 0.5$ can be observed.

Additionally, we show $D_{11}(r_x,0,r_z;z)$, $D_{22}(r_x,0,r_z;z)$ as functions of z for the same specified $z+r_z = 0.4\delta$ and for a fixed streamwise displacement r_x. The streamwise displacement value is chosen here such that the function $f(r_x) = \langle u(x,y,z)u(x+r_x,y,z+z_r) \rangle$ is at its maximum. We remark that this is in the spirit of the modulation model [41] in which the signal at the higher location is displaced in order to account for the lag between the "large-scale" signal (here at $z+r_z$) and the small-scale signal (here at z). As seen in Fig. 11, for the presently considered ranges of displacements, the shift in r_x does not affect the overall trends as a function of z, at least at this Reynolds number. It is worth noting that these structure functions do not vanish when $z \to 0$ (see Fig. 11 at small z^+) because the value at $z+r_z$ remains, i.e., $D_{11} = \langle [u(x,y,0) - u(x,y,r_z)]^2 \rangle = \langle u(x,y,z+r_z)^2 \rangle \neq 0$.

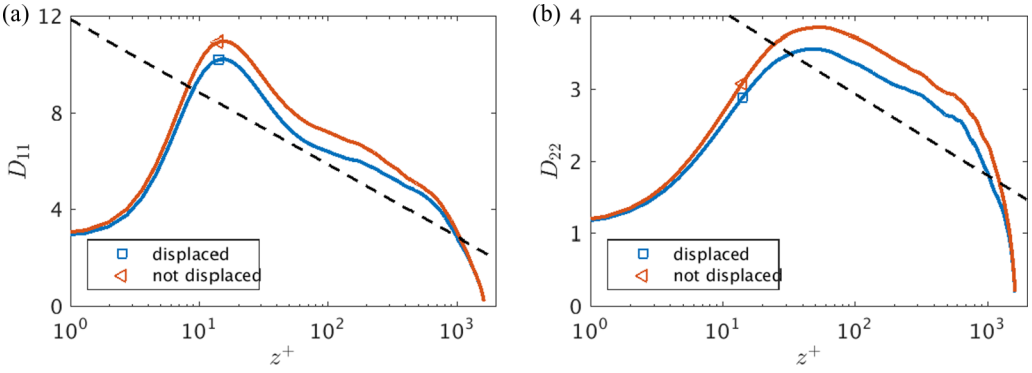

FIG. 11. Linear-log plot of $D_{11}(0,0,r_z;z)$, $D_{22}(0,0,r_z;z)$ as functions of z for fixed $z+r_z=0.4\delta$. The known slopes $A_1 \approx 1.25$, $A_{1,v}=0.5$ are indicated using dashed lines. We also show results for $D_{11}(r_x,0,r_z;z)$, and $D_{22}(r_x,0,r_z;z)$ where r_x is such that the function $f(r_x)=\langle u(x,y,z)u(x+r_x,y,z+r_z)\rangle$ is at its maximum. Results are denoted as "displaced."

To observe a logarithmic region, the HRAP formalism requires both z and $z+r_z$ to be in the logarithmic region. This is more easily attained for the spanwise component as $\langle vv\rangle$ has an extended logarithmic region, from $z^+\approx 50$ to $z/\delta\approx 0.4$) at this Reynolds number. If we consider $\langle v^2(z)\rangle=\langle[v(x,y,z)-0]^2\rangle=D_{22}(0,0,r_z>\delta;z)$, then in Fig. 11, we are simply taking $z+r_z$ from the freestream [where $v(z+r_z)=0$] to a wall-normal location in the boundary layer $(z+r_z)/\delta=0.4$. As is seen in Fig. 11(b), this reduces the logarithmic region to a range $50<z^+, z<0.4(z+r_z)$. The same does not hold for the streamwise component because a logarithmic region can barely be found in $\langle u^2\rangle$ at this Reynolds number. So it is interesting that when plotting D_{11} against z for $z+r_z=0.4\delta$, a logarithmic region begins to emerge, and more so for the displaced data, with the slope close to $A=1.25$.

Last we consider structure functions with displacements along a diagonal line on the x-y plane. Figure 12 shows D_{11}, D_{22} along a sample line that forms a $\sim 26^\circ$ angle with the x axis ($r_y/r_x=0.5$). As is expected from the HRAP model, logarithmic scalings are still found. Taking a diagonal line mixes the logarithmic scalings in the streamwise and spanwise directions. As a result, from the data the measured slopes are in between the slopes measured in the spanwise and streamwise directions. Recall that from HRAP the slopes would be expected to be equal for displacements in both directions

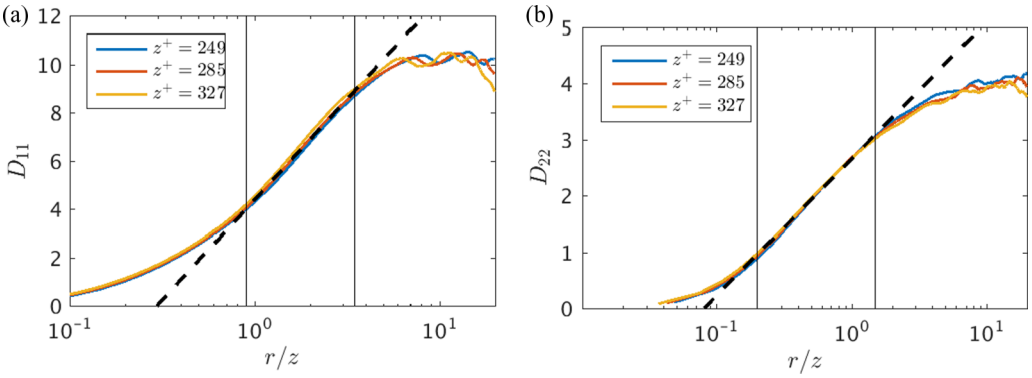

FIG. 12. Linear-log plot of $D_{11}(r_x,r_y,0,z)$, $D_{22}(r_x,r_y,0,z)$ for $r_y=r_x/2$ as a function of $r=\sqrt{r_x^2+r_y^2}$ at three wall-normal heights $z^+\approx 249,285,327$. The measured slopes are 3.6 and 1.1 for D_{11} and D_{22} and are indicated using dashed lines. Logarithmic scalings are observed within the region marked by vertical lines.

so the differences discussed previously in the context of the spanwise structure functions hold also for the present results.

V. CONCLUSIONS

In this work, we investigated the scaling behavior of the full structure function tensor [defined in Eq. (1)] in the logarithmic region within the framework provided by the HRAP, which is a simplified formalism based on the Townsend attached eddy hypothesis. The results for the required six scalar functions as a function of (r_x, r_y, r_z, z) are presented in Eqs. (18), (22), (24), (25), and (27). Certain special cases of Eq. (1) have been studied in the past, most notably the streamwise dependencies of the streamwise velocity component. In this paper, evidence supporting some of the newly proposed scalings is provided based on hot-wire and DNS data sets, in particular scaling that involves vertical displacements with respect to a fixed end point in the bulk region and logarithmic scaling for the transverse velocity component. However, the slope in the logarithmic laws for structure functions with displacements in the spanwise directions appeared to be larger than those predicted by the present simple version of HRAP. Several additional scalings laws remain to be confirmed in more detail and in laboratory experiments or DNS, which will need to be at higher Reynolds numbers than the ones that are presently available. The modeling work here thus calls for new detailed multipoint measurements of wall-bounded flows at high Reynolds numbers.

ACKNOWLEDGMENTS

The authors gratefully acknowledge A. Lozano-Duran for making the DNS data set available and for help accessing it. They acknowledge the financial support of the National Science Foundation, and the Australian Research Council.

---

[1] A. N. Kolmogorov, The local structure of turbulence in incompressible viscous fluid for very large Reynolds numbers, Dokl. Akad. Nauk SSSR **30**, 301-5 (1941).
[2] U. Frisch, *Turbulence: The Legacy of A. N. Kolmogorov* (Cambridge University Press, Cambridge, 1995).
[3] G. E. Karniadakis and K. S. Choi, Mechanisms of transverse motions in turbulent wall flows, Annu. Rev. Fluid Mech. **35**, 45 (2003).
[4] A. J. Smits, B. J. McKeon, and I. Marusic, High-Reynolds number wall turbulence, Annu. Rev. Fluid Mech. **43**, 353 (2011).
[5] I. Marusic, B. McKeon, P. Monkewitz, H. Nagib, A. Smits, and K. Sreenivasan, Wall-bounded turbulent flows at high Reynolds numbers: Recent advances and key issues, Phys. Fluids **22**, 065103 (2010).
[6] A. Townsend, *The Structure of Turbulent Shear Flow* (Cambridge University Press, Cambridge, 1976).
[7] A. E. Perry and I. Marusic, A wall-wake model for the turbulence structure of boundary layers. Part 1. Extension of the attached eddy hypothesis, J. Fluid Mech. **298**, 361 (1995).
[8] I. Marusic and A. E. Perry, A wall-wake model for the turbulence structure of boundary layers. Part 2. Further experimental support, J. Fluid Mech. **298**, 389 (1995).
[9] T. B. Nickels, I. Marusic, S. Hafez, N. Hutchins, and M. S. Chong, Some predictions of the attached eddy model for a high Reynolds number boundary layer, Philos. Trans. R. Soc. A **365**, 807 (2007).
[10] G. L. Eyink, Turbulent flow in pipes and channels as cross-stream "inverse cascades" of vorticity, Phys. Fluids **20**, 125101 (2008).
[11] I. Marusic, R. Mathis, and N. Hutchins, Predictive model for wall-bounded turbulent flow, Science **329**, 193 (2010).
[12] B. McKeon and A. Sharma, A critical-layer framework for turbulent pipe flow, J. Fluid Mech. **658**, 336 (2010).
[13] V. L. Thomas, B. K. Lieu, M. R. Jovanović, B. F. Farrell, P. J. Ioannou, and D. F. Gayme, Self-sustaining turbulence in a restricted nonlinear model of plane couette flow, Phys. Fluids **26**, 105112 (2014).

[14] J. Bretheim, C. Meneveau, and D. F. Gayme, Standard logarithmic mean velocity distribution in a band-limited restricted nonlinear model of turbulent flow in a half-channel, Phys. Fluids **27**, 011702 (2015).
[15] M. Hultmark, M. Vallikivi, S. C. C. Bailey, and A. J. Smits, Turbulent Pipe Flow at Extreme Reynolds Numbers, Phys. Rev. Lett. **108**, 094501 (2012).
[16] R. J. Stevens, M. Wilczek, and C. Meneveau, Large-eddy simulation study of the logarithmic law for second-and higher-order moments in turbulent wall-bounded flow, J. Fluid Mech. **757**, 888 (2014).
[17] K. Talluru, R. Baidya, N. Hutchins, and I. Marusic, Amplitude modulation of all three velocity components in turbulent boundary layers, J. Fluid Mech. **746**, R1 (2014).
[18] M. Lee and R. D. Moser, Direct numerical simulation of turbulent channel flow up to $\mathrm{Re}_\tau \approx 5200$, J. Fluid Mech. **774**, 395 (2015).
[19] G. J. Kunkel and I. Marusic, Study of the near-wall-turbulent region of the high-Reynolds-number boundary layer using an atmospheric flow, J. Fluid Mech. **548**, 375 (2006).
[20] C. de Silva, I. Marusic, J. Woodcock, and C. Meneveau, Scaling of second-and higher-order structure functions in turbulent boundary layers, J. Fluid Mech. **769**, 654 (2015).
[21] X. I. A. Yang, I. Marusic, and C. Meneveau, Hierarchical random additive process and logarithmic scaling of generalized high-order, two-point correlations in turbulent boundary layer flow, Phys. Rev. Fluids **1**, 024402 (2016).
[22] T. B. Nickels, I. Marusic, S. Hafez, and M. S. Chong, Evidence of the K_1^{-1} Law in a High-Reynolds-Number Turbulent Boundary Layer, Phys. Rev. Lett. **95**, 074501 (2005).
[23] C. Meneveau and I. Marusic, Generalized logarithmic law for high-order moments in turbulent boundary layers, J. Fluid Mech. **719**, R1 (2013).
[24] A. S. Monin and A. M. Yaglom, *Statistical Fluid Mechanics, Volume II: Mechanics of Turbulence* (Dover Publications, Inc., Mineola, NY, 2013).
[25] B. Vreman, B. Geurts, and H. Kuerten, Realizability conditions for the turbulent stress tensor in large-eddy simulation, J. Fluid Mech. **278**, 351 (1994).
[26] G. L. Eyink and H. Aluie, Localness of energy cascade in hydrodynamic turbulence. I. Smooth coarse graining, Phys. Fluids **21**, 115107 (2009).
[27] S. Cerutti and C. Meneveau, Statistics of filtered velocity in grid and wake turbulence, Phys. Fluids **12**, 1143 (2000).
[28] M. Wilczek, R. J. A. M. Stevens, and C. Meneveau, Spatio-temporal spectra in the logarithmic layer of wall turbulence: Large-eddy simulations and simple models, J. Fluid Mech. **769**, R1 (2015).
[29] M. Wilczek, R. J. A. M. Stevens, and C. Meneveau, Height-dependence of spatio-temporal spectra of wall-bounded turbulence–LES results and model predictions, J. Turbul. **16**, 937 (2015).
[30] C. Van Atta and W. Chen, Structure functions of turbulence in the atmospheric boundary layer over the ocean, J. Fluid Mech. **44**, 145 (1970).
[31] J. C. Kaimal, J. C. Wyngaard, D. A. Haugen, O. R. Coté, Y. Izumi, S. J. Caughey, and C. J. Readings, Turbulence structure in the convective boundary layer, J. Atmos. Sci. **33**, 2152 (1976).
[32] P. A. Davidson, T. B. Nickels, and P.-Å. Krogstad, The logarithmic structure function law in wall-layer turbulence, J. Fluid Mech. **550**, 51 (2006).
[33] R. J. Hill, Exact second-order structure-function relationships, J. Fluid Mech. **468**, 317 (2002).
[34] A. Cimarelli, E. De Angelis, J. Jimenez, and C. M. Casciola, Cascades and wall-normal fluxes in turbulent channel flows, J. Fluid Mech. **796**, 417 (2016).
[35] J. Jiménez, Cascades in wall-bounded turbulence, Annu. Rev. Fluid Mech. **44**, 27 (2012).
[36] I. Marusic, J. P. Monty, M. Hultmark, and A. J. Smits, On the logarithmic region in wall turbulence, J. Fluid Mech. **716**, R3 (2013).
[37] A. E. Perry and M. S. Chong, On the mechanism of wall turbulence, J. Fluid Mech. **119**, 173 (1982).
[38] J. C. Del Álamo, J. Jimenez, P. Zandonade, and R. D. Moser, Self-similar vortex clusters in the turbulent logarithmic region, J. Fluid Mech. **561**, 329 (2006).
[39] J. Woodcock and I. Marusic, The statistical behaviour of attached eddies, Phys. Fluids **27**, 015104 (2015).
[40] B. Ganapathisubramani, N. Hutchins, J. Monty, D. Chung, and I. Marusic, Amplitude and frequency modulation in wall turbulence, J. Fluid Mech. **712**, 61 (2012).

[41] R. Mathis, N. Hutchins, and I. Marusic, Large-scale amplitude modulation of the small-scale structures in turbulent boundary layers, J. Fluid Mech. **628**, 311 (2009).
[42] R. Mathis, N. Hutchins, and I. Marusic, A predictive inner–outer model for streamwise turbulence statistics in wall-bounded flows, J. Fluid Mech. **681**, 537 (2011).
[43] J. Gärtner, On large deviations from the invariant measure, Theory Probab. Appl. **22**, 24 (1977).
[44] R. S. Ellis, Large deviations for a general class of random vectors, Ann. Probab. **12**, 1 (1984).
[45] P. Moin, Revisiting Taylor's hypothesis, J. Fluid Mech. **640**, 1 (2009).
[46] C. Geng, G. He, Y. Wang, C. Xu, A. Lozano-Durán, and J. M. Wallace, Taylor's hypothesis in turbulent channel flow considered using a transport equation analysis, Phys. Fluids **27**, 025111 (2015).
[47] J. Kim, P. Moin, and R. Moser, Turbulence statistics in fully developed channel flow at low Reynolds number, J. Fluid Mech. **177**, 133 (1987).
[48] R. D. Moser, J. Kim, and N. N. Mansour, Direct numerical simulation of turbulent channel flow up to $\mathrm{Re}_\tau = 590$, Phys. Fluids **11**, 943 (1999).
[49] J. C. Del Alamo, J. Jiménez, P. Zandonade, and R. D. Moser, Scaling of the energy spectra of turbulent channels, J. Fluid Mech. **500**, 135 (2004).
[50] S. Hoyas and J. Jiménez, Scaling of the velocity fluctuations in turbulent channels up to $\mathrm{Re}_\tau = 2000$, Phys. Fluids **18**, 011702 (2006).
[51] A. Lozano-Durán and J. Jiménez, Effect of the computational domain on direct simulations of turbulent channels up to $\mathrm{Re}_\tau = 4200$, Phys. Fluids **26**, 011702 (2014).
[52] M. Bernardini, S. Pirozzoli, and P. Orlandi, Velocity statistics in turbulent channel flow up to $\mathrm{Re}_\tau = 4000$, J. Fluid Mech. **742**, 171 (2014).
[53] C. de Silva, D. Krug, D. Lohse, and I. Marusic, Universality of the energy-containing structures in wall-bounded turbulence, J. Fluid Mech. (unpublished).
[54] X. I. A. Yang, C. Meneveau, I. Marusic, and L. Biferale, Extended self-similarity in moment-generating-functions in wall-bounded turbulence at high Reynolds number, Phys. Rev. Fluids **1**, 044405 (2016).
[55] N. Hutchins, T. B. Nickels, I. Marusic, and M. S. Chong, Hot-wire spatial resolution issues in wall-bounded turbulence, J. Fluid Mech. **635**, 103 (2009).
[56] D. Squire, N. Hutchins, C. Morrill-Winter, M. Schultz, J. Klewicki, and I. Marusic, Applicability of Taylor's hypothesis in rough- and smooth-wall boundary layers, J. Fluid Mech. **812**, 398 (2017).
[57] A. E. Perry, S. Henbest, and M. S. Chong, A theoretical and experimental study of wall turbulence, J. Fluid Mech. **165**, 163 (1986).
[58] A. E. Perry and J. D. Li, Experimental support for the attached-eddy hypothesis in zero-pressure-gradient turbulent boundary layers, J. Fluid Mech. **218**, 405 (1990).
[59] N. Hutchins and I. Marusic, Large-scale influences in near-wall turbulence, Philos. Trans. R. Soc. A **365**, 647 (2007).